Nanoscale

Accepted Manuscript

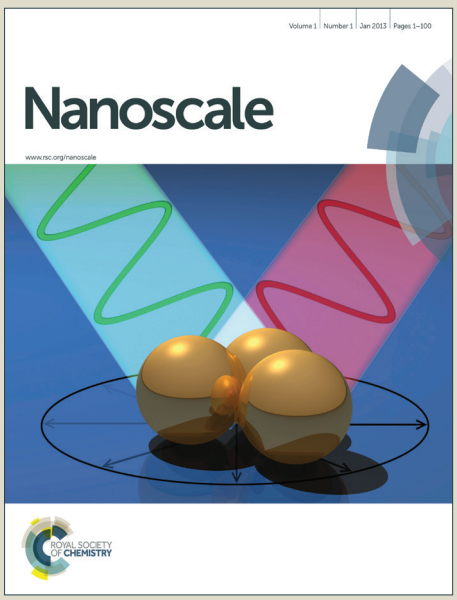

This is an *Accepted Manuscript*, which has been through the Royal Society of Chemistry peer review process and has been accepted for publication.

Accepted Manuscripts are published online shortly after acceptance, before technical editing, formatting and proof reading. Using this free service, authors can make their results available to the community, in citable form, before we publish the edited article. We will replace this *Accepted Manuscript* with the edited and formatted *Advance Article* as soon as it is available.

You can find more information about *Accepted Manuscripts* in the Information for Authors.

Please note that technical editing may introduce minor changes to the text and/or graphics, which may alter content. The journal's standard Terms & Conditions and the Ethical guidelines still apply. In no event shall the Royal Society of Chemistry be held responsible for any errors or omissions in this *Accepted Manuscript* or any consequences arising from the use of any information it contains.

ROYAL SOCIETY OF CHEMISTRY

www.rsc.org/nanoscale

Cite this: DOI: 10.1039/c0xx00000x

www.rsc.org/xxxxxx

ARTICLE TYPE

Enhancing the Performance of Photoelectrochemical Water Oxidation using Morphology-Controlled Indium Oxide Nanostructures that Grow Vertically on Fluorine-Doped Tin Oxide †

Changlong Chen,[a,b] Jonathon Moir,[a] Navid Soheilnia,[a] Benoit Mahler,[a] Laura Hoch,[a] Kristine Liao,[a] Veronika Hoepfner,[a] Paul O'Brien,[a] Chenxi Qian,[a] Le He[a] and Geoffrey A. Ozin*[a]

Received (in XXX, XXX) Xth XXXXXXXXX 20XX, Accepted Xth XXXXXXXXX 20XX
DOI: 10.1039/b000000x

Nanotower- and nanowall-like indium oxide structures were grown directly on fluorine-doped tin oxide (FTO)/In_2O_3 seeded substrates and pristine FTO substrates, respectively, by a straightforward solvothermal method. The tower-like nanostructures are proposed to form via a self-assembly process on the In_2O_3 seeds. The wall-like nanostructures are proposed to form via epitaxial growth from the exposed edges of SnO_2 crystals of the FTO substrate. The nanotowers and nanowalls reveal highly crystalline and ordered nanocrystals with preferred orientations in the [111] and [110] directions, respectively. The two structures display remarkably different activities when used as photoanodes in solar light-driven water splitting. X-ray photoelectron spectroscopy results suggest an increased density of hydroxyl groups in the nanowalls, which results in a decrease in the work function and a concomitant shift in the onset potential of photocurrent in the linear sweep voltammograms, which is further confirmed by Mott-Schottky and flat-band potential measurements, indicating the importance of hydroxyl content in determining the photoelectrochemical properties of the films. Morphology-controlled, nanostructured transparent conducting oxide electrodes of the kind described in this communication are envisioned to provide valuable platforms for supporting catalysts and co-catalysts that are intentionally tailored for efficient light-assisted oxidation of water and reduction of carbon dioxide.

Introduction

Environmental problems resulting from the combustion of non-renewable fossil fuels have compelled scientists to focus on exploring green and renewable alternative energy sources. Photoelectrochemical (PEC) water splitting using semiconductor materials to produce hydrogen and oxygen has attracted much attention due to its potential to efficiently utilize solar energy to produce usable fuels.[1] In practical PEC devices, it is essential for the semiconductor to be stable in the electrolyte and possess high efficiency in catalyzing the photon-to-hydrogen/oxygen conversion.[2,3] In terms of stability, metal oxide semiconductors are the most suitable materials for PEC electrodes as most of them possess exceptionally high resistances to photocorrosion.[4] Many metal oxide semiconductors such as TiO_2,[5,6] WO_3,[7,8] Fe_2O_3,[9,10] ZnO[11] and $BiVO_4$[2,12] have long been studied as potential photoanode materials for PEC devices.

However, most metal oxide semiconductors typically display low quantum efficiencies due to the short diffusion lengths of charge carriers.[4,10] This is a result of the nature of the energy bands in metal oxides,[13] as well as trap states within the crystal structures that act as recombination centers.[4] As a result, only holes created in a region very close to the surface of metal oxide photoanodes can diffuse to the material/electrolyte interface and oxidize water, which means that the majority of holes created in the bulk of the material will be lost through recombination before reaching the interface.[10] In this regard, thin films should be superior to thick films when used as photoelectrodes in PEC systems. Conversely, thinner films absorb less light due to their shorter optical path length. Therefore, the ideal material maximizes both the absorption of incident light as well as the number of photogenerated charge carriers that can diffuse to the electrode/electrolyte interface.

An effective synthetic strategy to achieve this goal is the fabrication of photoelectrodes using nanostructured films instead of dense, planar films. Typical examples are the vertically grown one-dimensional TiO_2[14–18] and ZnO[19,20] nanorod and nanowire arrays, which exhibit significantly enhanced photoelectrochemical properties when compared to their corresponding planar structures. Similarly, branched or dendritic semiconductor nanostructures vertically grown on substrates are known to be good candidates for PEC devices.[10,21–24] Due to their open structure, vertically aligned nanostructured films not only provide much larger surface areas, but also enable a greater fraction of the photogenerated minority carriers to diffuse to the electrode/electrolyte interface, thus facilitating charge separation and reducing electron-hole pair recombination.[23,24] In addition, electron transport between the material and the substrate is improved significantly due to the direct growth of the photoactive

Nanoscale Accepted Manuscript

component on the electrode.[14] In this regard, high surface area semiconductor nanostructured photoelectrodes vertically grown on transparent conductive substrates are expected to significantly enhance PEC device efficiency.

Indium oxide (In_2O_3) is a well-known metal oxide semiconductor material with a band gap ranging from 2.8 eV to 3.6 eV.[25,26] The superior conductivity and stability of In_2O_3 as well as its suitable valence band edge for water oxidation make it a very interesting material for PEC water splitting.[27] In our previous work, In_2O_3 nanowalls were grown on tin doped indium oxide (ITO) substrates via an epitaxial growth mechanism.[28] FTO is a commonly used transparent conductive oxide (TCO) substrate often superior in PEC devices due to its high stability.[29] However, direct growth of In_2O_3 on FTO is very challenging because of the large lattice mismatch between In_2O_3 and SnO_2, and to our knowledge such configurations have not been previously reported.

In this work, we report two new synthetic strategies to achieve vertically grown indium oxide nanostructures, denoted nanotowers and nanowalls, on FTO substrates. Films were characterized by scanning electron microscopy (SEM), transmission electron microscopy (TEM), selected area electron diffraction (SAED) and powder X-ray diffraction (pXRD). Their photoelectrochemical activities were evaluated using linear sweep voltammetry (LSV) under simulated sunlight (AM1.5G, 1 sun). Differences in activity between the two morphologies were correlated to changes in X-ray photoelectron spectroscopy (XPS) binding energies and results from electrochemical impedance spectroscopy (EIS) measurements.

Experimental

Materials: Indium (III) acetate (99.99%), indium (III) chloride (98%), thioacetamide (98%) and urea (98%) were purchased from Sigma-Aldrich. Acetic acid (99.7%) and anhydrous ethanol were purchased from Caledon and Commercial Alcohols, respectively. All of chemicals were used as received. Glass slides coated with fluorine-doped tin oxide (FTO, Tec 15) were purchased from Hartford Glass Company, Inc.

Growth of Nanostructures on FTO: In_2O_3 nanowalls were grown on FTO by a seed induced method. Firstly, indium sulfide (In_2S_3) nanocrystals were synthesized via a microwave method: 0.2920 g of indium (III) acetate and 0.1465 g of thioacetamide were dissolved into a solution composed of 15 mL of deionized water and 1 mL of acetic acid and then heated rapidly in a microwave reactor (Discover SP microwave reactor, CEM Corporation) to 140 ℃ with 200 W full power and maintained at 140 ℃ for 1 h. The product was allowed to cool to room temperature and washed three times with de-ionized water and two times with ethanol. The particles were then dispersed in ethanol to form a suspension with a concentration of about 4.0 mg/mL. A drop of the suspension was spin-coated onto an FTO slide at 3000 rpm in order to seed the substrate with the In_2S_3. The seeded FTO substrate was heated at 10 ℃/min to a temperature of 600 ℃ and annealed at 600 ℃ for 30 min in order to convert the sample to In_2O_3/FTO.

To grow nanotower-like In_2O_3 on FTO, a solvothermal process was employed. Before the solvothermal reaction, the Teflon-lines of the autoclaves were soaked in dilute HCl for 2 h, washed with deionized water and ethanol and dried under a flow of air. In a typical synthesis, 0.0442 g of indium(III) chloride and 0.15 g of urea were ultrasonically dissolved in 30 mL of anhydrous ethanol. After adding 20 μL of deionized water, the solution was poured into the Teflon-lined stainless steel autoclave (50 mL volume). One piece of the FTO/In_2O_3 seeded substrate was placed at an angle against the wall of the Teflon-liner. The solvothermal reaction was conducted at 190 ℃ for 24 h.

To grow In_2O_3 nanowalls on FTO, pristine FTO substrates were placed into autoclaves as described above. Except for the reaction temperature and time - which were 170 ℃ and 48 h, respectively - the reaction solution loaded in the autoclave was identical with that adopted for the nanotower-like In_2O_3 growth.

As a control, In_2O_3 powder films deposited on FTO were fabricated. Specifically, In_2S_3 thin films were firstly fabricated by spin coating using the same In_2S_3 suspension that was used to fabricate the seeded substrate in the In_2O_3 nanotower preparation. The In_2S_3 was then converted to In_2O_3 by annealing the In_2S_3 films at 600 ℃. By controlling the number of drops of the suspension in the spin-coating process, the net load of the In_2O_3 film on the FTO could be controlled.

Characterization: Scanning electron microscopy (SEM) and energy-dispersive X-ray spectroscopy (EDX) analyses of the samples were performed on a FEI Quanta FEG 250 environmental scanning electron microscope at an accelerating voltage of 10 kV. The SEM samples were adhered onto stubs using carbon tape and reinforced using carbon paste. Transmission electron microscopy (TEM, Hitachi H-7000) with an accelerating voltage of 100 kV was used to examine the fine structure of the nanowalls and nanotowers, and to conduct the selected area electron diffraction (SAED). Powder X-ray diffraction (pXRD) patterns were recorded on a Bruker D2 Phaser diffractometer (Cu Kα radiation) with a fixed voltage of 30 kV and a current of 10 mA at ambient temperature. UV-Vis absorption spectra were measured using a Perkin-Elmer Lambda 1050 UV/VIS/NIR spectrometer equipped with an integrating sphere. The percent of absorbed light (A) was calculated by measuring the percent of transmitted (T) and reflected (R) light, such that A=100–T–R. X-ray photoelectron spectroscopy (XPS) was performed using a Perkin Elmer Phi 5500 ESCA spectrometer. The Al Kα X-ray source was operated at 15 kV and 27 A with X-ray wavelengths of 1486.7 eV. All measurements were carried out in an ultrahigh vacuum chamber with a base pressure of 10^{-9} Torr. The Multipak program was used for all data analysis. The NIST-XPS database and the *Handbook of X-ray Photoelectron Spectroscopy* were used as references for binding energy.[30,31] Ultraviolet Photoelectron Spectroscopy (UPS) was used for valence band and work function measurements. The UV photons (at 21.22 eV) for UPS measurements were generated by helium plasma at a back pressure of 2×10^{-5} Torr. The UPS measurements were performed under the same vacuum condition as the XPS measurements. Samples used for UPS measurements were prepared the same way as in the XPS measurements.

Photoelectrochemical (PEC) and incident photon to charge conversion efficiency (IPCE) Measurements: PEC measurements utilized simulated sunlight obtained by passing light from a 150 W Xe arc lamp (Newport 67005) through an AM1.5G filter (Newport 81094) and calibrating the output to one

Nanoscale Accepted Manuscript

This journal is © The Royal Society of Chemistry year

sun (100 mW/cm^2) using a reference cell and power meter (Oriel 91150V). Linear sweep voltammetry (LSV) was performed using a Solartron SI 1287 Electrochemical Interface in a three-electrode configuration, with the semiconductor film as the working electrode, a Hg/HgO (20 wt% KOH, Koslow Scientific) reference electrode and a Pt wire counter electrode. A 0.1 M aqueous solution of NaOH was used as the electrolyte. For ease of comparison with other literature reports, the measured potentials vs. Hg/HgO were converted to the reversible hydrogen electrode (RHE) scale according to the Nernst equation:

$$E_{RHE} = E_{Hg/HgO} + 0.059\ pH + E^{\theta}_{Hg/HgO} \quad (1)$$

where E_{RHE} is the converted potential vs. RHE, $E^{\theta}_{Hg/HgO}$ = +0.098 V at 25 ℃ and $E_{Hg/HgO}$ is the experimentally measured potential against the Hg/HgO reference electrode.

IPCE measurements were performed using monochromatic light (monochromator, Newport 74100) and an applied potential of 1.40 V (vs. RHE) using the same electrochemical setup described above. The intensity of the monochromatic light was calibrated using a power meter (Thorlabs, PM100D) with a S120VC Si detector. The IPCE can be expressed by the equation:

$$\mathrm{IPCE} = \frac{1240I}{\lambda J_{\mathrm{light}}} \quad (2)$$

where I (in mA/cm^2) is the measured photocurrent density at a specific wavelength, λ (in nm) is the wavelength of incident light and J_{light} (in mW/cm^2) is the measured irradiance at a specific wavelength.

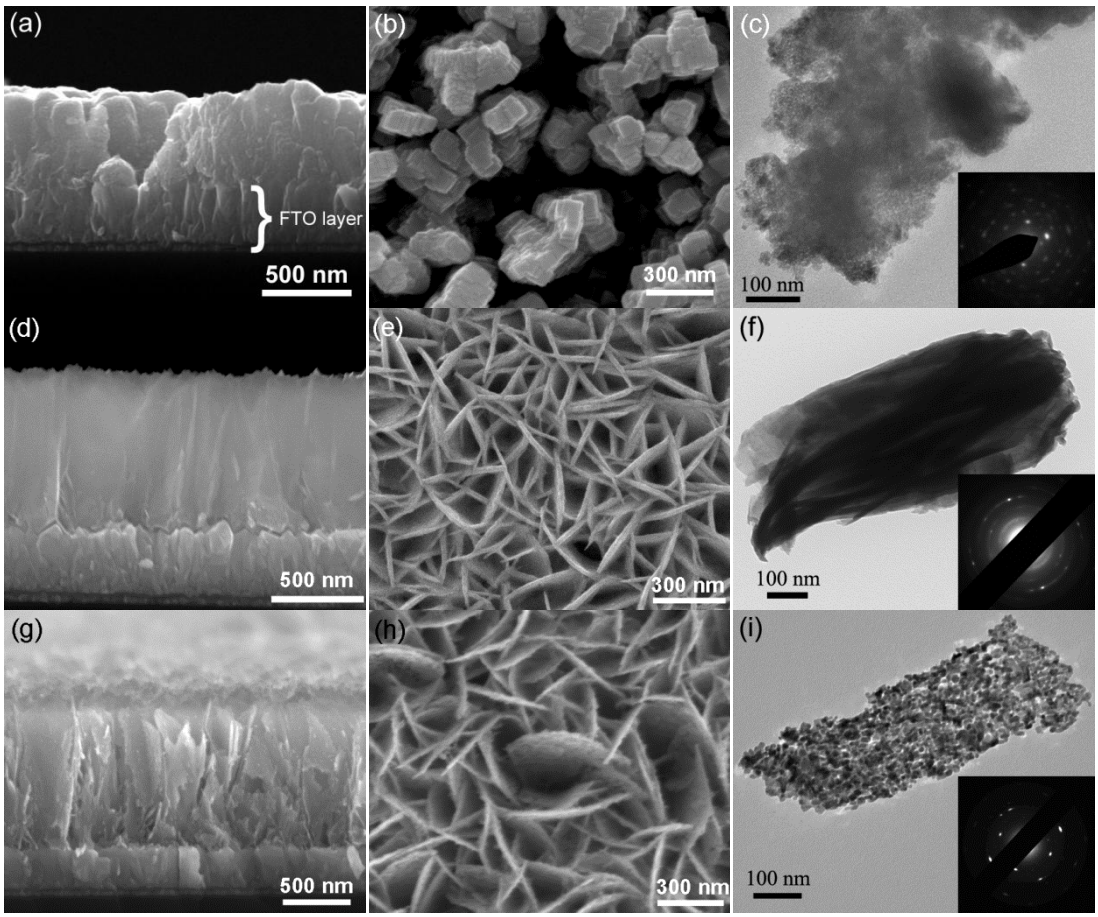

Fig. 1 SEM images of indium oxide nanotowers (a-b), as-synthesized nanowalls (d-e) and nanowalls after heat treatment (g-h). (a,d,g) are cross-sectional views and (b, e, h) are top-views of the samples. (c, f, i) are the TEM images of the indium oxide nanotowers, as-synthesized nanowalls and nanowalls after heat treatment, respectively, in which the SAED patterns of the corresponding samples are shown in the insets.

Electrochemical impedance spectroscopy (EIS) Measurements: EIS measurements were performed using a Solartron SI 1287 Electrochemical Interface coupled with a Solartron SI 1260 Impedance/Gain-Phase Analyzer, using the same three-electrode configuration described above but with a Ag/AgCl reference electrode (BASi) in place of the Hg/HgO electrode. The applied potential was converted to the RHE scale using equation (1) but in this case using the reference potential for the Ag/AgCl electrode ($E^{\theta}_{Ag/AgCl}$ = +0.197 V at 25 ℃). The frequency range was between 10^5 Hz – 0.1 Hz. The magnitude of the alternating signal was +/-10 mV. The EIS measurements were performed in 0.1M NaOH solution in the dark. Nyquist plots were fitted using ZPlot software (Scribner) and were modeled using a simple Randles' equivalent circuit.[32,33] In this equivalent circuit, R_S is the series resistance through the system and R_{CT} is the resistance to charge transfer across the semiconductor-liquid junction. The capacitance was actually measured as a constant phase element (CPE), however the exponential parameter was

Nanoscale Accepted Manuscript

found to be > 0.86 at all potentials, and the CPE was therefore approximated as a pure capacitance.

Results and Discussion

Nanotower- and nanowall-like In_2O_3 structures were grown directly on FTO/In_2O_3 seeded substrates and pristine FTO substrates, respectively, by a straightforward solvothermal method (see the detailed experimental processes in ESI†). Fig. 1a-b show scanning electron microscopy (SEM) images of the nanotower In_2O_3 structures grown on the seeded FTO substrate at 190 ℃ for 24 h (an SEM image of the seeded substrate is provided in ESI, Fig. S1a†). These nanotowers have irregular top cross-sections with area sizes ranging from 80×100 to 200×500 nm^2 and are distributed uniformly on the substrate with distances of no more than 300 nm apart (ESI, Fig. S2a† for zoomed out view of Fig. 1b). Fig. 1b shows that each In_2O_3 nanotower is composed of smaller "bricks". The edges and corners of these small bricks can be observed clearly. The film thickness, i.e., the height of the nanotowers, is ~ 500 nm as determined from the cross-section image in Fig. 1a. Due to the thickness of the nanotowers, it was difficult to acquire a clear TEM image. Fig. 1c shows the TEM image of one fragment of a nanotower that was obtained by extended ultrasonication of a nanotower sample scraped from an FTO substrate. The corresponding SAED pattern of this fragment is shown in the inset of Fig. 1c, and reveals the crystalline nature of the nanotowers. The crystal phase and its orientation with respect to the substrate were confirmed by using powder X-ray diffraction (pXRD) and Rietveld refinement of the resulting diffraction pattern. As shown in Fig. 2a, the pXRD pattern of the tower-like In_2O_3 on FTO exhibits two sets of diffraction peaks. One set of peaks originates from the FTO substrate, which can be confirmed by the pXRD pattern of the pristine FTO substrate. The other set of peaks can be indexed to cubic indium oxide (JCPDS 65-3170, bottom of Fig. 2). No peaks belonging to phases other than these two materials were observed, indicating that the nanotower structures grown on FTO are cubic In_2O_3. The Rietveld-refinement of the diffraction pattern of the nanotowers is shown in Fig. 2c (see detailed information in the ESI†), and indicates a slight preference for growth of the towers in the [111] crystal direction normal to the substrate.

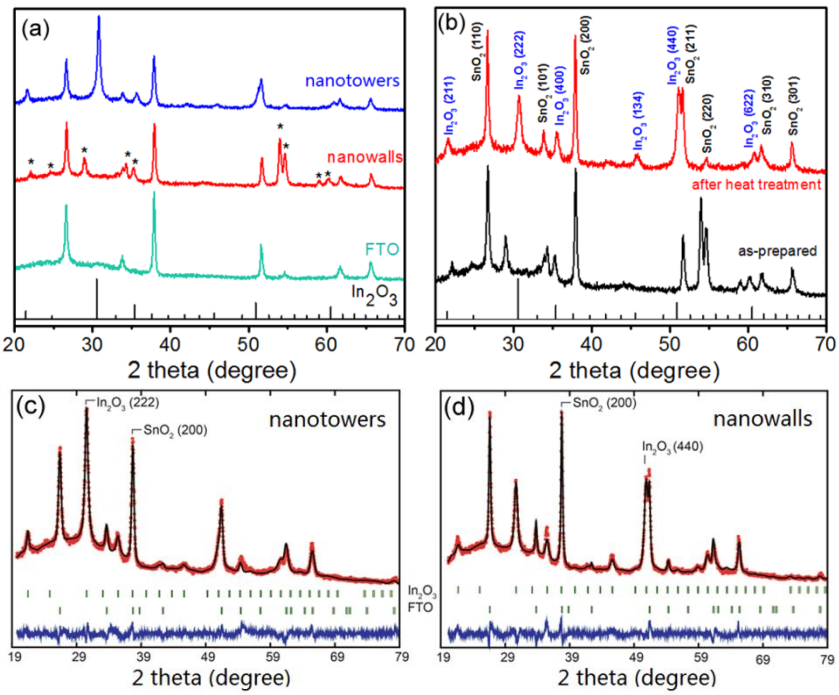

Fig. 2 (a) pXRD patterns of the pristine FTO substrate and the as-prepared indium oxide nanotowers and nanowalls grown on FTO. (b) pXRD patterns of the nanowalls grown on FTO before and after heat treatment at 460 ℃. The bar-chart at the bottom of both plots indicates the diffraction peaks of In_2O_3 (JCPDS 65-3170). The final Rietveld refinement plot of the (c) nanotower In_2O_3 (R_P = 3.81; R_{Bragg} = 4.92) and (d) heat-treated nanowall In_2O_3 nanostructures (R_P = 4.12; R_{Bragg} = 6.18) are provided, showing the observed (red) and calculated (black) patterns as well as their difference (blue). Green bars indicate the calculated Bragg peaks for both the In_2O_3 cubic phase and the SnO_2 phase (FTO substrate). For both patterns the (*hkl*) reflections that suggest a preferred orientation in the films are indicated.

Nanostructures grown on pristine FTO, i.e. without In_2O_3 seeds, were shown to have a nanowall morphology. Fig. 1d-e show the SEM images of the nanowalls prepared at 170 ℃ for 48 h. They reveal that the film is composed of vertically aligned nanosheets, which are distributed uniformly on the substrate and form a cross-linked nanowall network (ESI, Fig. S2b† for a zoomed-out view). The nanosheets have a width of ~ 300 nm and a thickness of 15-20 nm (a higher magnification SEM image is shown in ESI, Fig. S1b†). The cross-sectional image (Fig. 1d) shows that the nanosheets are about 860 nm high and are vertically aligned on the FTO layer. Fig. 1f shows a TEM image of the nanosheets and their SAED pattern (inset), in which the lamellar and crystalline nature of the nanosheets is clearly shown. Further analysis using pXRD is shown in Fig. 2a, which shows diffraction peaks associated with the FTO substrate in addition to diffraction peaks (marked with stars) which cannot be indexed to any known indium oxide, (oxy)hydroxide or hydroxide crystal phase. It is speculated that the as-prepared nanowalls are an intermediate

Nanoscale Accepted Manuscript

This journal is © The Royal Society of Chemistry year

phase or a precursor of the typical In_2O_3.

To further investigate the structure of the nanowalls we first performed energy-dispersive X-ray spectroscopy (EDX), which revealed that chlorine is present in the nanowalls in addition to oxygen and indium (ESI, Fig. S3†), indicating that the nanowalls are a complex phase rather than simply indium oxide, (oxy)hydroxide, or hydroxide. Intensive investigations on the composition and crystal phase of this intermediate product will be carried out in future work. Secondly, we performed heat-treatments on the nanowall samples. Specifically, at a heating rate of 1 ℃/min in air, the nanowalls were heated to 460 ℃ and held at that temperature for 1.5 h and then cooled to ambient temperature. As shown in Fig. 2b, after heat treatment, the sample possesses the characteristic diffraction pattern of cubic bixbyite In_2O_3. Rietveld-refinement of the diffraction pattern (Fig. 2d) indicates a strong diffraction peak associated with the (440) crystal face, indicating that the preferred orientation of the nanostructures is in the [110] direction normal to the substrate. Apart from In_2O_3 and FTO, no other diffraction peaks are found from the pXRD pattern of the heat-treated sample. This indicates that the as-prepared nanowall sample is an intermediate phase or a precursor of the typical In_2O_3 that can be transformed into stable cubic In_2O_3 via heat treatment. The SEM images of the heat-treated nanowalls shown in Fig. 1g-h reveal that the nanowall morphology is maintained after the heat treatment and the nanosheets become slightly thinner, with thicknesses of ~ 10 nm. The top-view and cross-sectional SEM images with lower magnification (ESI, Fig. S2c† and S4†) show that the nanowall layer on FTO is uniform. Moreover, during the SEM measurements, it was found that the as-prepared nanowalls exhibited obvious charging effects under the electron beam but that the heat-treated nanowalls showed good conductivity, indicating good stability following treatment. Fig. 1i shows the TEM image of one piece of the heat-treated nanosheet, showing that the nanosheet is composed of small 10 nm crystals. This crystal size corresponds with the thickness of the nanosheets observed by SEM (Fig. 1h), indicating that the nanosheet is composed of only one layer of nanocrystals. In addition, the SAED pattern of the nanosheets shows a well-defined set of diffraction spots typical for single crystals (inset of Fig. 1i), indicating that all crystals in the nanosheet share the same orientation.

Further experiments were carried out to investigate the growth process of the nanostructures on FTO. It was found that the reaction temperature played a key role in the formation of the different morphologies of the indium oxide nanostructures. For the nanowalls, a reaction temperature of no higher than 180 ℃ is necessary, otherwise large particles rather than nanowalls form on the substrate (see an example of a sample that was formed at 190 ℃, ESI, Fig. S5a†). On the other hand, decreasing the reaction temperature will increase the time needed for the formation of the nanowalls. For example, at a temperature of 140 ℃, a reaction time longer than 48 h is needed for the detection of diffraction peaks at 2θ = 54.0 ° and 54.6 °, the two strongest diffraction peaks for the intermediate phase of the nanowalls. This result indicates the embryonic growth stage of the nanowalls, as evident from the change in the XRD pattern. For the nanotowers grown on seeded FTO substrates, the reaction temperature must be ≥190°C. When the temperature is lower than 190 ℃, nanowalls form together with large and irregular particles (ESI, Fig. S5b†). However the pXRD pattern for this lower temperature synthesis confirms the formation of cubic In_2O_3 (ESI, Fig. S6†). Based on these detailed experiments and analysis, we propose a probable growth mechanism of the as-synthesized nanostructures: the nanotowers are formed by a self-assembly process on the In_2O_3 seeds; the nanowalls are formed *via* epitaxial growth from the exposed edges of SnO_2 crystals of the FTO (ESI, Growth Mechanism†).

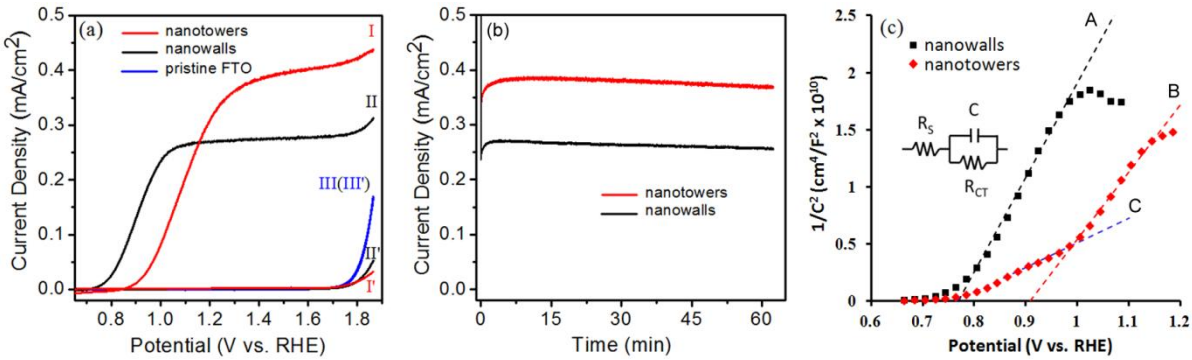

Fig. 3 (a) LSV collected from In_2O_3 nanotowers and nanowalls and pristine FTO samples under AM1.5G illumination at 100 mW/cm^2 (I, II, III) and in the dark (I', II', III'). (b) Photocurrent density vs. time of the In_2O_3 nanotowers and nanowalls obtained at 1.40 V (vs. RHE) under AM 1.5G illumination at 100 mW/cm^2. (c) Mott-Schottky plots of the nanowall and nanotower films, derived from the capacitance values shown in ESI, Fig. S7† using equation (3). The Randles' equivalent circuit model used to fit the data is shown as an inset, where R_S is the series resistance through the system, R_{CT} is the resistance to charge transfer across the semiconductor liquid junction, and C is the capacitance within the space charge region of the semiconductor. A, B, C are fitted lines from the linear portions of the Mott-Schottky plots.

Using a standard three-electrode configuration, with a Hg/HgO (20 wt% KOH) reference electrode and a platinum wire counter electrode, the In_2O_3 nanostructures grown on FTO were investigated as working electrodes for PEC water splitting. To compare the PEC performance of the two nanostructures, the nanotowers were heat treated under the same conditions as the nanowalls (460 ℃ for 1.5 h). Powder XRD patterns and SEM images reveal that the nanotowers did not exhibit any changes after the heat treatment. Linear sweep voltammograms were collected in 0.1 M NaOH aqueous solution under simulated sunlight (100 mW/cm^2) using an AM1.5G filter. Fig. 3a shows the linear sweep voltammograms (LSV) of the In_2O_3 nanowalls

Nanoscale Accepted Manuscript

and nanotowers both in the dark and under illumination. As can be seen from red curve I in the figure., the photocurrent density of the In_2O_3 nanotowers exhibits an onset potential of ~ 0.85 V (vs. RHE, all potentials appearing hereafter are relative to RHE), at which point the photocurrent increases steeply with increasing applied potential. After a potential of about 1.30 V, a plateau photocurrent density of ~ 0.4 mA/cm^2 is achieved. At this point, bulk recombination of photoexcited charges limits the overall photoactivity.[2] In the dark, the nanotower sample shows negligible current density (< 1 μA/cm^2, red curve I' in Fig. 3a) up to 1.70 V, indicating that the charge transfer is prevented due to the overpotential required to initiate water oxidation. This is commonly observed for metal oxide photoanodes.[1] In addition, the stability of the nanostructures in the PEC process was also studied. As shown in Fig. 3b, the two samples possess a relatively good photostability, showing a decay of only ~ 4.4% in 60 minutes. At the same time, further analyses by SEM and XRD techniques revealed that both the morphology and crystal structure of the two samples were unchanged following the PEC measurements.

For the In_2O_3 nanowalls, the photocurrent onset occurs at a potential of ~ 0.75 V (Fig. 3a, black curve II), which is negatively shifted by ~ 0.1 V compared to the nanotower sample. The photocurrent density also rises rapidly to a plateau photocurrent of ~ 0.26 mA/cm^2 at potentials > 1.1 V. The current density observed in the dark (Fig. 3a, black curve II') almost overlaps with that of the In_2O_3 nanotowers. As a control, the PEC performance of a pristine FTO substrate was also evaluated. As seen from Fig. 3a (blue curve III and III'), the pristine FTO does not show currents up to 1.7 V both under dark and under AM1.5G illumination (100 mW/cm^2) conditions, indicating the importance of the In_2O_3 structures in the photoelectrochemically-driven water splitting process.

Table 1 Flat-band potentials and donor densities for the three linear portions of the Mott-Schottky plots in Fig. 3c.

Sample	Line	Flat-band potential (V_{FB} vs. RHE)	Donor density (N_D, in cm^{-3})
nanowalls	A	+0.74	4.2×10^{20}
nanotowers	B	+0.88	6.0×10^{20}
nanotowers	C	+0.74	1.6×10^{21}

To evaluate the difference in onset potential between the two nanostructured films, Mott-Schottky plots (Fig. 3c) were constructed from the capacitance values derived from electrochemical impedance spectroscopy (EIS) measurements. The capacitance plotted as a function of potential is shown in ESI, Fig. S7†. The inverse of the capacitance squared is plotted as a function of applied potential and shown in Fig. 3c. From the figure a linear relationship is observed and can be modeled using the Mott-Schottky equation:[34-37]

$$\frac{1}{C^2} = \frac{2}{q\varepsilon\varepsilon_0 N_D}\left[V - V_{FB} - \left(\frac{kT}{q}\right)\right] \quad (3)$$

where C is the capacitance (in F/cm^2), q is the elementary charge (1.60×10^{-19} C), ε is the relative dielectric constant of In_2O_3 (taken to be 4),[38-40] ε_0 is the permittivity of free space (8.854×10^{-14} F/cm), N_D is the donor density (in cm^{-3}), V is the applied potential (vs. RHE), V_{FB} is the flat-band potential (vs. RHE), k is Boltzmann's constant (1.38×10^{-23} C· V/K) and T is the temperature (298 K). Fig. 3c shows the linear portions of the Mott-Schottky plots and Table 1 summarizes the flat-band potentials (V_{FB}) and donor densities (N_D) derived from these linear plots. It is clear that the onset potentials for photocurrent observed in Fig. 3a match the flat-band potentials measured using EIS. Specifically, the flat-band potential of the nanowalls was found to be + 0.74 V (line A), whereas the flat-band potential of the nanotowers was found to be + 0.88 V (line B). We note a second linear portion of the Mott-Schottky plot observed for the nanotowers (line C), which results in a flat-band potential that matches that of the nanowalls. However, the photocurrent onset does not occur at this potential. It is possible that the presence of multiple dopants (hydroxyls, oxygen vacancies, chloride ions, etc) could explain the presence of two linear segments with differing slopes.[41] It is also possible that there are multiple crystal facets exposed to the electrolyte solution, and that each crystal facet exhibits a different work function and surface structure, which will ultimately affect the onset potential and the kinetic activity of the sample.[42,43] However, in the Rietveld-refinement (Fig. 2c and 2d) only the nanowalls showed a strong preferred orientation; the nanotowers exhibited only a weakly preferred orientation. From this information, and based on the TEM image in Fig. 1i, it is clear that the nanowalls are composed of many smaller isotropic nanocrystals, which should allow for many different facets to interact with the electrolyte. It would therefore be expected that the nanowalls, and not the nanotowers, should exhibit multiple linear regions in the Mott-Schottky plot. As such, it seems unlikely that different exposed crystal facets would create the observed bifurcation.

Table 2 Work function and valence band maximum determined from XPS and UPS measurements, respectively.

Sample	Work Function (V vs. RHE)		Valence Band (V vs. RHE)	
	XPS	UPS	XPS	UPS
nanowalls	0.58	0.36	3.57	3.53
nanotowers	0.74	0.46	3.52	3.57

The most likely reason for a shift in onset potential is a difference in overall work function between the two films. To investigate this further XPS measurements were performed in order to determine the work function and valence band maximum (VBM) energy levels of the nanowalls and nanotowers. Table 2 summarizes the results of the XPS measurements for the Fermi level (work function) and the VBM as determined from the secondary electron cut-off and the onset of photoemission, respectively. The values have been converted to the RHE scale in order to compare them to the onset potentials determined from LSV and EIS measurements. It is clear that the nanowalls exhibit a smaller work function than the nanotowers by ~ 0.16 V (vs. RHE), consistent with the results of the LSV and EIS measurements. The reason for this shift is apparent in the core binding energies for the O1s photoemission peaks. Fig. 4a shows the normalized O1s photoemission peaks for the two samples, whereas Fig. 4b and 4c show the deconvolution of these peaks for the nanowalls and nanotowers, respectively. The main peak is associated with In-O-In lattice oxygen atoms in the cubic In_2O_3 structure, whereas the shoulder peak is associated with hydroxyl

Nanoscale Accepted Manuscript

This journal is © The Royal Society of Chemistry year

groups and oxygen vacancies present within the structure.[25,44] From the deconvolution of the peaks, it appears that the nanotowers have a slightly greater number of oxygen vacancies than the nanowalls. However, this apparent difference is likely not significant because the donor densities of both materials are very similar (Table 1). Oxygen vacancies generally function as n-type donors in metal oxide materials so a substantial increase in oxygen vacancy concentration should result in a significant increase in donor density.[45] The deconvolution of the O1s peaks also indicates that the nanowalls contain a greater number of hydroxyl groups than the nanotowers; the ratio of peak areas for In-O-In to In-OH is 1:0.9 for the nanowalls compared to 1:0.5 for the nanotowers. It is possible that this difference could account for the decrease in the measured work function for the nanowalls. The VBM would not be expected to change dramatically, due to the low lying energy levels of lattice hydroxyl species that are well below the VBM.[15] Indeed, both samples have very similar VBM energies (Table 2). Additionally, a shift in photoemission peak position is observed for the nanowalls both in the O1s region (Fig. 4a) and in the In3d region (ESI, Fig. S8†). This would also be consistent with the presence of hydroxyl groups, which would act as electron withdrawing groups and shift the binding energies of both the oxygen and indium atoms in the lattice.

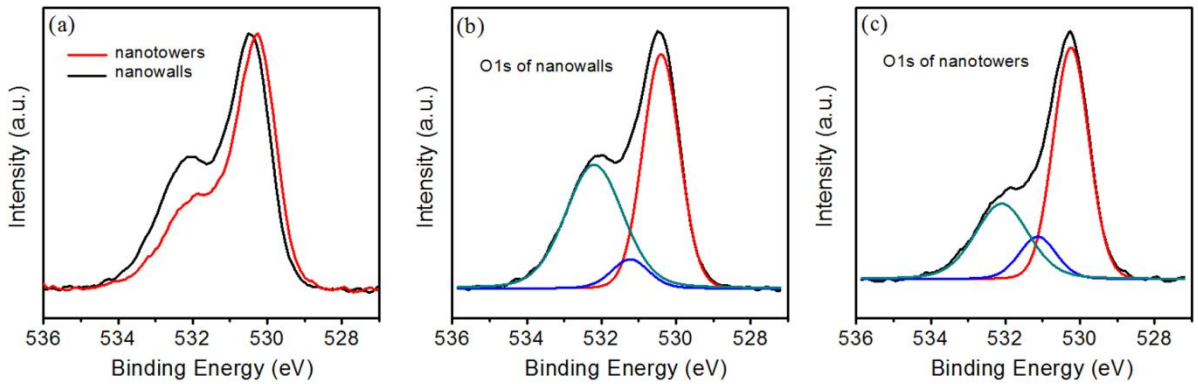

Fig. 4 (a) O1s core level photoemission spectra for the nanowalls and nanotowers. (b,c) Deconvolution of the O1s peaks for the nanowall and nanotower samples; the peaks shown in red, green and blue color belong to In-O-In lattice oxygen, hydroxyl groups and oxygen vacancies, respectively; the ratios of In-O-In to In-OH peak areas for nanowall sample and nanotower sample are 1:0.9 and 1:0.5, respectively.

Table 2 also shows the work function and VBM data obtained from UPS measurements. Again, there is very little difference in the VBM of both samples however it is interesting to note that the work functions for both samples are slightly closer in energy than those measured with XPS, which probes deeper into the sample. Because UPS is a much more surface-sensitive technique, the fact that the work function values are closer suggests that the surfaces of both the nanowalls and nanotowers are similarly hydroxylated and that the main difference between the two samples is the bulk hydroxyl content. This might also explain the two separate onsets in the Mott-Schottky plots in Fig. 3c. The difference in hydroxyl content between the two samples may be related to the different synthetic procedures. The nanotowers directly form as In_2O_3 during the hydrothermal synthesis, while the nanowalls form a complex precursor phase during the hydrothermal step and only form In_2O_3 after calcination at 460 ℃. This complex precursor likely consists of multiple hydroxide species and its decomposition could result in residual hydroxyl species within the bulk crystal.

We note that while the nanowalls exhibit an earlier onset potential for photocurrent, the nanotowers exhibit a much higher plateau photocurrent at potentials > 1.2 V. A variety of factors could affect the observed discrepancy in photocurrent between the two morphologies in this region. In order to narrow this down, we first looked at the absorption properties of the two films tested electrochemically. An increase in absorption could result in an increase in photocurrent. We therefore measured the reflection and transmission spectra (shown in ESI, Fig. S9† and S10†, respectively) of the two samples using an integrating sphere and calculated the percent of absorbed photons for each sample from these measurements, as described in the Experimental section. The absorption spectra in Fig. 5a show that the nanotowers absorb more light than the nanowalls throughout the visible spectrum and a significant portion of the UV spectrum. This increased absorption is attributed to enhanced light scattering from the nanotowers as compared to the nanowall structure. This effect is manifest in the transmission spectra (ESI, Fig. S10†), which show transmission through the nanowall structure is greater than through the nanotower sample. Furthermore, Fabry-Perot fringes, reminiscent of reflection from homogeneous transparent thin films, can be identified in the reflection spectra from the nanowall structure (ESI, Fig. S9†). On the other hand, on account of increased internal light scattering, Fabry-Perot fringes are not apparent in the reflection spectra from the nanotower sample. It can also be noted that the nanotower sample appears visually opaque compared to the more transparent nanowall sample.

While light absorption is greater in the nanotower sample, IPCE measurements shown in Fig. 5b indicate that photoactivity does not occur at wavelengths > 400 nm, which is consistent with the direct-forbidden band gap of In_2O_3.[25,26] Conversely, increased absorption for wavelengths in the spectral region 300 nm < λ < 400 nm leads to increased photoactivity in the nanotower sample. However, in comparing the absorption spectra (Fig. 5a) to the IPCE spectra (Fig. 5b) it is apparent that other factors must also contribute to the enhanced photoactivity in the nanotower sample. For example, at a wavelength of λ = 325 nm absorption in the two samples is comparable, however the IPCE of the nanotower

Nanoscale Accepted Manuscript

sample is approximately twice that of the nanowall sample. In this context, we performed additional experiments to further investigate why the nanotowers exhibit a substantially higher photoactivity than the nanowalls for photons with wavelength less than 350 nm, despite comparable absorption in the two structures.

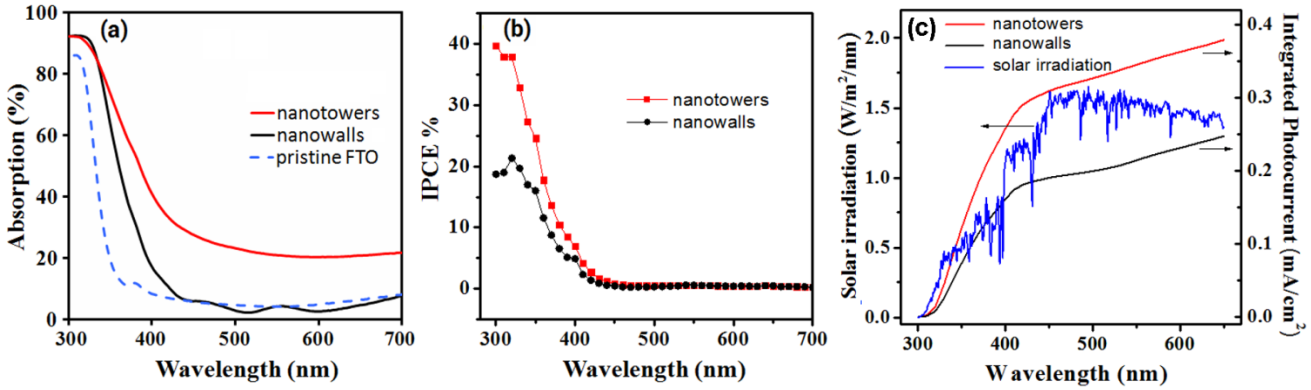

Fig. 5 (a) Percent of absorbed photons vs. wavelength for the nanotowers, nanowalls and the pristine FTO samples. The percent of absorbed photons for each sample was calculated from the percent of reflected photons (ESI, Fig. S9†) and the percent of transmitted photons (ESI, Fig. S10†). (b) IPCE spectra of the In_2O_3 nanotowers and nanowalls collected at a potential of 1.40 V. (c) Standard AM 1.5G solar spectrum (ASTM G-173-03, blue color) and simulated total photocurrents of the In_2O_3 nanotowers and nanowalls as a function of wavelength. The simulated photocurrents were obtained by integrating the IPCE spectra collected at 1.40 V with the standard AM 1.5G solar spectrum.

To rule out differences in charge transport through the nanotower and nanowall structures, the series resistance through the films (measured using EIS) was analyzed as a function of applied potential. The contributions from the electrochemical equipment and solution resistance to the series resistance have been found to be negligible. As the same reference electrode and solution were used to measure both samples, any differences in series resistance would likely stem from the semiconductor nanostructures. ESI, Fig. S11† shows the series resistance as a function of applied potential for the two samples. While the nanotowers exhibit a slightly lower series resistance at higher applied potentials, this difference is not sufficient to explain the ~ 1.4 fold increase in photoactivity under high positive bias. More complex models were attempted in order to fit the data, including a transmission line model.[36,46,47] Unfortunately the models were unable to fit the data. This is likely due to the very efficient transport of charge through the nanostructures and the lack of a transmission line in the Nyquist plots.

Since charge transport changes could not explain the increased photocurrent in the nanotower sample, we ultimately considered surface area as the most likely enhancement mechanism. While gas adsorption measurements could be used to determine differences in surface area of the two morphologies, this would also include semiconductor material that is not electrochemically accessible and would give skewed results. We therefore used the electrochemical capacitance of the films as a measure of their surface area. ESI, Fig. S7† shows the capacitance values as a function of applied potential for the nanowalls and nanotowers, as derived using EIS. The inset shows a zoom-in of the potential region where the plateau photocurrent is observed in Fig. 3a. In this region, the applied bias is high enough that the space-charge region of the semiconductor adjacent to the electrolyte is heavily depleted, resulting in charge separation efficiencies close to unity. The resulting photocurrent becomes solely limited by bulk recombination in the semiconductor and exhibits a plateau. For two nanostructures that are composed of the same cubic structure and have nearly identical charge transport properties, the amount of semiconductor exposed to electrolyte (i.e. the electrochemically active surface area) will therefore determine the maximum photocurrent output. From the inset in ESI, Fig. S7†, it is clear that the nanotowers exhibit a ~ 1.4 fold increase in capacitance compared to the nanowall sample. Given that the two samples have identical geometric surface areas (3 cm^2), it would appear that the difference in real surface areas is responsible for the difference in photocurrent output.

Additionally, based on the IPCE data and the standard AM 1.5G solar spectrum (ASTM G-173-03),[48] the total photocurrent of the nanotowers and nanowalls under simulated global sunlight can be obtained by integrating the IPCE spectra according to equation (4): [10,15]

$$\int I(\lambda)\mathrm{d}\lambda = \int \frac{IPCE(\lambda)\cdot E(\lambda)\cdot\lambda}{1240}\mathrm{d}\lambda \qquad (4)$$

where $E(\lambda)$ (in mW/cm^2/nm) is the solar irradiance at a specific wavelength λ (in nm). The solar photocurrent calculated according equation (4) is independent of the light source and applied filters, and is therefore more accurate in evaluating the water splitting performance of the films. As shown in Fig. 5c, the simulated photocurrents of the In_2O_3 nanotowers and nanowalls at 1.40 V as a function of wavelength between 300 to 650 nm are 0.37 and 0.25 mA/cm^2, respectively, which closely match the photocurrents measured in the PEC cell under simulated sunlight (Fig. 3a, values of 0.38 and 0.27 mA/cm^2 for the nanotowers and nanowalls, respectively).

Conclusions

In summary, In_2O_3 nanostructures with nanotower and nanowall morphologies were directly grown on FTO substrates using new synthetic methods. The straightforward growth of oxide semiconductor nanostructures on conductive oxide substrates allows for enhanced electrical contact with the substrates. When used as photoanodes for PEC water splitting, the In_2O_3

Nanoscale Accepted Manuscript

This journal is © The Royal Society of Chemistry year

nanotowers and nanowalls both showed considerable photocurrents under AM 1.5G simulated solar irradiation. The nanowalls exhibited an earlier photocurrent onset than the nanotowers, which was confirmed to coincide with a more negative flat-band potential. The reason for this shift originated from a decrease in the work function of the nanowalls as compared to the nanotowers, and was suggested to be a result of an increase in hydroxyl content within the films. The nanotowers exhibited a much higher photocurrent output at high positive potentials. Electrochemical impedance spectroscopy measurements suggested that this improvement was primarily due to an increase in surface area. These results suggest the merits of combining nanostructuring and increased surface area, with tailored compositions of dopants in semiconductors, which can simultaneously decrease the applied energy required for photocurrent onset and maximize the total photocurrent output under depletion conditions. Such morphology controlled, nanostructured transparent conducting oxide electrodes are envisioned to provide valuable platforms for supporting catalysts and co-catalysts that are intentionally tailored for efficient light-assisted oxidation of water and reduction of carbon dioxide, the subject of ongoing investigations in our solar fuels laboratory.

Acknowledgements

GAO is Government of Canada Tier 1 Canada Research Chair in Materials Chemistry and Nanochemistry. Strong and sustained financial support of this solar fuels research from the Ontario Ministry of Research and Innovation (MRI), the Ontario Ministry of Economic Development and Innovation (MEDI), the Natural Sciences and Engineering Council of Canada (NSERC) and the University of Toronto are deeply appreciated. CC appreciates the financial support for his visiting professorship provided by the University of Jinan. JM is grateful for an NSERC CGS award. In addition, the authors wish to thank Ilya Gourevich in the Chemistry Department at University of Toronto for technical assistance with electron microscopy measurements.

Notes and references

[a] *Department of Chemistry, University of Toronto, Toronto, Ontario, M5S3H6, Canada. E-mail: gozin@chem.utoronto.ca*
[b] *School of Chemistry and Chemical Engineering, University of Jinan, Jinan, Shandong, 250022, P R China.*

† Electronic Supplementary Information (ESI) available: Growth mechanism, EDX analysis, XRD pattern and SEM images of indium oxide nanostructures, SEM images of pristine FTO, illustration of the quasi-epitaxial growth mechanism of oriented nanocrystal indium oxide nanowalls on a FTO substrate, $In3d_{5/2}$ core binding energies for the two nanostructured films, transmission and reflection spectra, series resistance and capacitance as a function of potential for the two In_2O_3 nanostructured films. See DOI: 10.1039/b000000x/

1. K. Sivula, *J. Phys. Chem. Lett.*, 2013, **4**, 1624–1633.
2. J. A. Seabold and K.-S. Choi, *J. Am. Chem. Soc.*, 2012, **134**, 2186–2192.
3. M. Higashi, K. Domen and R. Abe, *J. Am. Chem. Soc.*, 2012, **134**, 6968–6971.
4. L. C. Schumacher, S. Mamiche-Afara, M. Leibovitch and M. J. Dignam, *J. Electrochem. Soc.*, 1988, **135**, 3044–3050.
5. B. Chen, J. Hou and K. Lu, *Langmuir*, 2013, **29**, 5911–5919.
6. P. Hartmann, D.-K. Lee, B. M. Smarsly and J. Janek, *ACS Nano*, 2010, **4**, 3147–3154.
7. Q. Chen, J. Li, X. Li, K. Huang, B. Zhou, W. Cai and W. Shangguan, *Environ. Sci. Technol.*, 2012, **46**, 11451–11458.
8. C. Santato, M. Ulmann and J. Augustynski, *J. Phys. Chem. B*, 2001, **105**, 936–940.
9. R. S. Schrebler, L. Ballesteros, A. Burgos, E. C. Mun, P. Grez, D. Leinen, F. Martı and E. A. Dalchiele, *J. Electrochem. Soc.*, 2011, **158**, D500–D505.
10. A. Kay, I. Cesar and M. Grätzel, *J. Am. Chem. Soc.*, 2006, **128**, 15714–15721.
11. A. Wolcott, W. A. Smith, T. R. Kuykendall, Y. Zhao and J. Z. Zhang, *Adv. Funct. Mater.*, 2009, **19**, 1849–1856.
12. K. Sayama, A. Nomura, T. Arai, T. Sugita, R. Abe, M. Yanagida, T. Oi, Y. Iwasaki, Y. Abe and H. Sugihara, *J. Phys. Chem. B*, 2006, **3**, 11352–11360.
13. H. Sun, W. Fan, Y. Li, X. Cheng, P. Li and X. Zhao, *J. Phys. Chem. C*, 2010, **114**, 3028–3036.
14. B. Liu and E. S. Aydil, *J. Am. Chem. Soc.*, 2009, **131**, 3985–3990.
15. G. Wang, H. Wang, Y. Ling, Y. Tang, X. Yang, R. C. Fitzmorris, C. Wang, J. Z. Zhang and Y. Li, *Nano Lett.*, 2011, **11**, 3026–3033.
16. Y. J. Hwang, A. Boukai and P. Yang, *Nano Lett.*, 2009, **9**, 410–415.
17. X. Feng, K. Shankar, O. K. Varghese, M. Paulose, T. J. Latempa and C. A. Grimes, *Nano Lett.*, 2008, **8**, 3781–3786.
18. S. Hoang, S. Guo, N. T. Hahn, A. J. Bard and C. B. Mullins, *Nano Lett.*, 2012, **12**, 26–32.
19. M. Law, L. E. Greene, J. C. Johnson and R. Saykally, *Nature*, 2005, **4**, 455–459.
20. X. Yang, A. Wolcott, G. Wang, A. Sobo, R. C. Fitzmorris, F. Qian, J. Z. Zhang and Y. Li, *Nano Lett.*, 2009, **9**, 2331–2336.
21. J. B. Baxter and E. S. Aydil, *Appl. Phys. Lett.*, 2005, **86**, 053114.
22. K. Pan, Y. Dong, W. Zhou, Q. Pan, Y. Xie, T. Xie, G. Tian and G. Wang, *ACS Appl. Mater. Interfaces*, 2013, **5**, 8314–8320.
23. A. Kargar, K. Sun, Y. Jing, C. Choi, H. Jeong, G. Y. Jung, S. Jin and D. Wang, *ACS Nano*, 2013, **7**, 9407–9415.
24. I. S. Cho, Z. Chen, A. J. Forman, D. R. Kim, P. M. Rao, T. F. Jaramillo and X. Zheng, *Nano Lett.*, 2011, **11**, 4978–4984.
25. C. Janowitz, V. Scherer, M. Mohamed, A. Krapf, H. Dwelk, R. Manzke, Z. Galazka, R. Uecker, K. Irmscher, R. Fornari, M. Michling, D. Schmeißer, J. R. Weber, J. B. Varley and C. G. Van De Walle, *New J. Phys.*, 2011, **13**, 085014.
26. A. Walsh, J. L. F. Da Silva, S.-H. Wei, C. Korber, A. Klein, L. F. J. Piper, A. DeMasi, K. E. Smith, G. Panaccione, P. Torelli, D. J. Payne, A. Bourlange and R. G. Egdell, *Phys. Rev. Lett.*, 2008, **100**, 167402.
27. B. Zhang, N. N. Zhang, J. F. Chen, Y. Hou, S. Yang, J. W. Guo, X. H. Yang, J. H. Zhong, H. F. Wang, P. Hu, H. J. Zhao and H. G. Yang, *Sci. Rep.*, 2013, **3**, 3109.
28. C. Chen, Y. Wei, G. Sun and B. Shao, *Chem. Asian J.*, 2012, **7**, 1018–1025.
29. R. Bel, H. Tahar, T. Ban, Y. Ohya and Y. Takahashi, *J. Appl. Phys.*, 1998, **83**, 2631.
30. A. V. Naumkin, A. Kraut-Vass, S. W. Gaarenstroom and C. J. Powell, "NIST X-ray Photoelectron Spectroscopy Database," can be found under http://srdata.nist.gov/xps/Default.aspx, **2012**.
31. J. F. Moulder, W. F. Stickle, P. E. Sobol and K. D. Bomben, *Handbook of X-ray Photoelectron Spectroscopy*, Physical Electronics, Inc., Eden Prairie, Minnesota, USA, **1995**.
32. C. Y. Cummings, F. Marken, L. M. Peter, K. G. U. Wijayantha and A. A. Tahir, *J. Am. Chem. Soc.*, **2012**, *134*, 1228–1234.
33. B. Klahr, S. Gimenez, F. Fabregat-Santiago, J. Bisquert and T. W. Hamann, *Energy Environ. Sci.*, **2012**, *5*, 7626–7636.
34. K. Rajeshwar, *Encycl. Electrochem.*, 2007, 1–51.
35. A. W. Bott, *Curr. Sep.*, 1998, **17**, 87–91.
36. K. Gelderman, L. Lee and S. W. Donne, *J. Chem. Educ.*, 2007, **84**, 685–688.
37. B. M. Klahr, A. B. F. Martinson and T. W. Hamann, *Langmuir*, 2011, **27**, 461–8.
38. A. A. Dakhel, *Chem. Phys. Lett.*, 2004, **393**, 528–534.
39. A. Walsh and D. O. Scanlon, *Phys. Rev. B*, 2013, **88**, 161201.
40. P. Reunchan, X. Zhou, S. Limpijumnong, A. Janotti and C. G. Van de Walle, *Curr. Appl. Phys.*, 2011, **11**, S296–S300.
41. I.-H. Toor, *J. Electrochem. Soc.*, 2011, **158**, C391–C395.

Nanoscale Accepted Manuscript

42. L. F. Zagonel, M. Bäurer, A. Bailly, O. Renault, M. Hoffmann, S.-J. Shih, D. Cockayne and N. Barrett, *J. Phys. Condens. Matter*, 2009, **21**, 314013.
43. A. Imanishi, H. Suzuki, K. Murakoshi and Y. Nakato, *J. Phys. Chem. B*, 2006, **110**, 21050–21054.
44. W.-C. Chang, C.-H. Kuo, C.-C. Juan, P.-J. Lee, Y.-L. Chueh and S.-J. Lin, *Nanoscale Res. Lett.* 2012, **7**, 684.
45. F. A. Peter Atkins, T. Overton, J. Rourke and M. Weller, *Shriver & Atkins Inorganic Chemistry*, W. H. Freeman And Company, New York, NY, 2006.
46. J. Bisquert and A. Compte, *J. Electroanal. Chem.*, 2001, **499**, 112–120.
47. J. Bisquert, *J. Phys. Chem. B*, 2002, **106**, 325–333.
48. http://rredc.nrel.gov/solar/spectra/am1.5/astmg173/astmg173.html.

Nanoscale Accepted Manuscript

This journal is © The Royal Society of Chemistry year